Final Review

Dottorato in fisica teorica XXXII ciclo
Dip. di Fisica “M.Merlin” Bari
Supervisor: Prof. Giuseppe Gonnella, Dott. Antonio Lamura

Giuseppe Negro

October 14, 2019

1 Introduction

In this brief review I will report on the research activity that I carried on during my PhD. Our work is mainly concerned with the modellization and numerical simulation of Biological fluids, like suspensions of biological filaments such as actomyosin, mictrotubules bundles activated with kinesin motors and bacterial cultures, which are "active" and evolve far from thermodynamic equilibrium. In fact they are internally driven by continuous injection of energy at the level of the individual constituents. Among the variety of biological process, cell motion is one of the most fascinating. Understanding how cells move around their surroundings has gained much attention in the recent past, mainly because answering this question would constitute a substantial step-forward in dissecting the fundamental mechanisms underlying biomedical problems like wound-healing and tissue self-assembly during embryogenesis [1]. Spontaneous movement and deformation are physically driven by the cell cytoskeleton. The cytoskeleton consists of protein filaments and motors which constantly consume chemical energy (ATP) and convert it to work. In particular, actin filaments interact with myosin motors to generate contraction forces in the cell, which can drive cell motion and division [2, 3].

Most of the research has focused, both experimentally and theoretically, on cells migration on a two-dimensional substrate (crawling) [4, 5], mainly because such experimental systems are easily accessible hence this motion is more readily observable. These studies have stimulated the development of theories which now provide a detailed outline of some basic migration mechanisms, including the formation of lamellipodia arising from actin polymerization at the cell front, adhesion-mediated traction, and actomyosin contractility. The crawling motility mode requires actin cytoskeleton to be anchored to the substrate throughout focal adhesions, that are clusters of trans-membrane proteins binding to the substrate [6]. However some cells, such as breast tumor cells, can also “swim” in a straight line inside a 3D tissue or a polymeric fluid [7]. Unlike cell crawling, in this case there is no solid surface present, and no cellular protrusion reminiscent of a lamellipodium (the cell shape instead remains roughly spherical). The lack of protrusions suggests that actin polymerisation may not be crucial for 3D cell swimming. Indeed, myosin motors contraction is believed to be the sole responsible for cell polarisation and motility [7]: together with some experiments on tumor cells [8], this observation suggests that cell swimming may be primarily driven by myosin activity.

In this review we will first present results regarding a minimal scalar model to study the role of compressibility in cell motion.

Experiments on concentrated suspensions of bacteria or cytoskeletal extracts have shown that active systems often exhibit orientational order. Indeed they have been successfully modelled by Liquid Crystal (LC) theories, able to reproduce unexpected behaviors arising in active fluids, such as spontaneous flow, active turbulence and superfluidic states [9]. Although chirality is an ubiquitous feature of biological matter, its role in many biological processes, including which motion, has not been extensively studied yet. Left-right asymmetry may be due to thermodynamic (passive) or non-equilibrium (active) effects. For instance, flagella of some bacteria, acto-myosin filaments as well as microtubule bundles are all examples of intrinsically chiral systems that may eventually apply a non equilibrium active torque on the surrounding fluid environment, thus leading to motility. Despite much effort has been taken to understand the hydrodynamics of active nematic/polar fluids in bidimensional environments, much less is known about chiral systems and in general about active matter in three dimensional geometries [10]. In the second part of this review we will present some results regarding a system which is inherently chiral and apolar and that can be modelled - in the passive limit - as a Cholesteric Liquid Crystal (CLC). Specifically we examined the behavior of a 3D CLC droplet with tangential anchoring of the director at its surface. Previous studies on achiral (nematic) shell showed that activity can only sustain oscillatory motion of topological defects on the surface, while motility of polar droplet is driven by symmetry breaking of its shape [11]. Our results show that intrinsically chiral droplets display instead a much richer dynamical behavior, and we will review some of them in the second part of this assay.

2 Hydrodynamics of contraction-based motility in a compressible active fluid

Models of contraction-induced motility have been proposed in Refs. [11, 12, 13, 14]. All these considered the case of an active droplet moving inside a simple (Newtonian) and passive outer fluid. In some cases, the material inside the droplet was an active liquid crystal, in which case the onset of motility required rectifications of orientational splay fluctuations of an order parameter linked to actin polarisation [11, 12]. Instead we study by lattice Boltzmann simulations a simpler, single-phase, compressible actomyosin system, where a high density droplet (actomyosin blob) simply emerges due to active contraction. For sufficiently strong activity, we find the self-assembled droplet swims inside a low density actomyosin background. The setup we consider could be studied experimentally with quasi-2D or 3D compressible actomyosin suspensions. Additionally, once the droplet emerges, the system is approximately equivalent to an active compressible actomyosin droplet swimming inside a generic compressible and passive fluid (as the density of motors in the background is very small). Therefore, our results can be qualitatively compared to experiments studying the motion of cells or cell extracts within polymeric or viscoelastic fluids. Indeed, we show that the hydrodynamic flows in the region outside the droplet are reminiscent of the flow of matrigel [1] surrounding swimming cells.

2.1 Hydrodynamic model

We model an actin suspension as a compressible fluid with local density ρ, and myosin via its concentration field ϕ. Rather than considering the case in which actin is enclosed in a droplet [14],

[1] At least at large times, matrigel can be viewed as a viscous fluid rather than a solid.

we study a single-fluid set-up with a compressible actin gel initially uniform in the simulation domain. The dynamical equation of motion for the actin density ρ is the continuity equation,

$$\partial_t \rho + \partial_\alpha \rho v_\alpha = 0 \ , \tag{1}$$

with v_α the velocity of the actin fluid. The latter obeys the following Navier-Stokes momentum balance equation,

$$\partial_t \rho v_\alpha + \partial_\beta (\rho v_\alpha v_\beta) = F_\alpha^{\rm int} + F_\alpha^{\rm active} + F_\alpha^{\rm interface} + F_\alpha^{\rm viscous} \ , \tag{2}$$

where $F_\alpha^{\rm viscous} = \partial_\beta [\eta(\partial_\beta v_\alpha + \partial_\alpha v_\beta)]$ is the usual viscous term, with η shear viscosity of the fluid. The term

$$F_\alpha^{\rm int} = -\partial_\alpha P^i + \partial_\alpha G \rho \ , \tag{3}$$

accounts for pressure-driven flows. The quantity $P^i = \rho T$ is the usual ideal pressure. The presence of the additional term proportional to G gives a compressibility proportional to $T - G$. Hence G measures the deviation from the ideal behaviour of the fluid, being temperature fixed in our simulations. The third term

$$F_\alpha^{\rm interface} = k \rho \partial_\alpha (\nabla^2 \rho) \tag{4}$$

represents interfacial forces, with the constant k controlling the surface tension of actin (which controls the width of interfaces between high and low actin densities). The presence of the active component (myosin motors with local density ϕ), and its effects on the fluid, are encoded in the final term,

$$F_\alpha^{\rm active} = \zeta \partial_\alpha \phi \ , \tag{5}$$

which accounts for an active isotropic pressure – if $\zeta > 0$ this active pressure is contractile. The parameter ζ measures the strength of myosin-induced contraction. Contractility depends also on the concentration of myosin motors ϕ, which evolves according to the following advection-diffusion equation:

$$\partial_t \phi + \nabla.(\phi \mathbf{v}) = D \nabla^2 \phi - B \nabla^2 \rho - K (\nabla^2)^2 \phi \ . \tag{6}$$

Here the local advection velocity of myosin equals that of actin, meaning that all motors are permanently attached to the actomyosin gel. The parameter D is the myosin diffusion coefficient, while K controls the myosin surface tension, quantifying the ability of the myosin droplet to oppose deformation. The term proportional to B is an effective non-equilibrium term, whose effect is to ensure that myosin remains enclosed in actin domains. Higher order gradients terms can in principle be added, but they would not alter the following results. The study is conducted by varying G ("compressibility modulus") and the activity parameter ζ.

The equations of motion are solved by means of a hybrid lattice Boltzmann (LB) scheme, as the one described in chapter LB.

Simulations have been performed on a periodic square lattice of size $L = 128$, for the 2D case, and a periodic cubic lattice of size $L = 128$ for 3D simulations. Unless otherwise stated, initial conditions are $\phi = 1$ inside a droplet of radius $R_1 = 3$, and 0 outside , while ρ set equal to $\rho = 1$ inside a droplet of radius $R_2 = 15$, and $\rho = 0.4$ elsewhere. Parameter values are, $T = 0.97$, $k = 0.1$, $D = 10^{-3}$, $B = D$, $K = 10^{-3}$. All quantities in the text are reported in lattice (simulation) units.

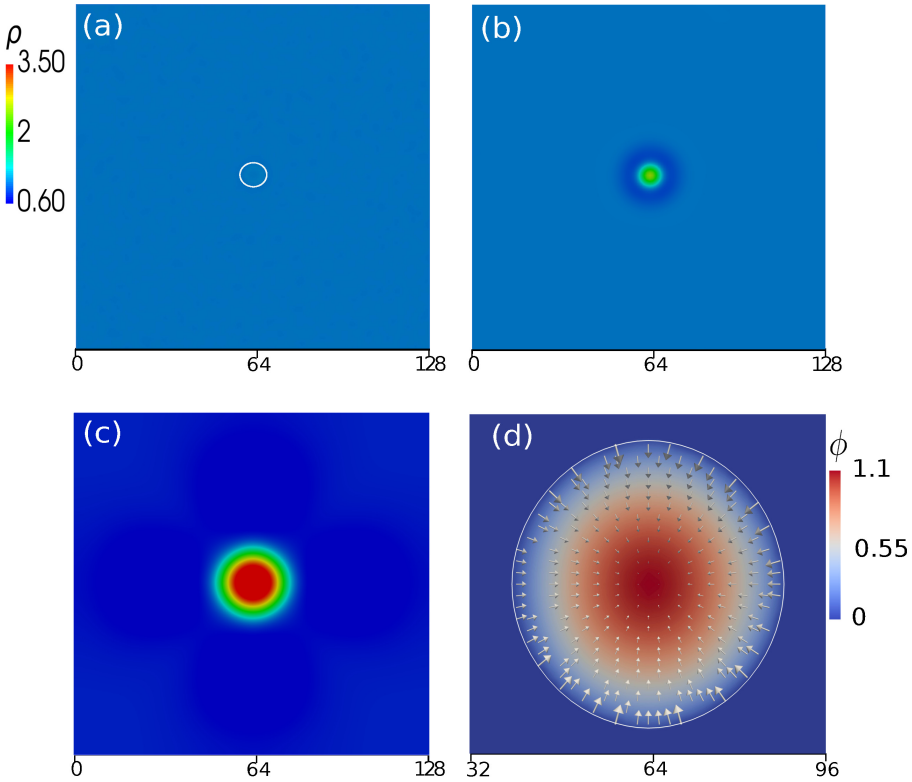

Figure 1: **(a-c)** Snapshots of the evolution of ρ, for a simulation in which ρ has been initialized randomly around 1(panel (a)), while ϕ as a droplet of radius $R = 3$ (isoline for $\phi = 1$ in panel (a)), for $\zeta = 0.1$ and $G = 0.95$. **(d)** Contour plot of ϕ with superimposed active force, for the same configuration shown in (c). The isoline for $\rho = 2$ is plotted in white.

2.2 Results

We start by presenting the results of our 2D simulations.

The first finding is that contractility alone is able to create a droplet of active fluid (actin, represented by ρ) even in the absence of a free energy favouring phase separation in the passive limit ($\zeta = 0$). Initialising the system with $\rho = \rho_0 + \delta\rho$, where $\rho_0 = 1$ and $\delta\rho$ some small random fluctuations, whereas ϕ (motor concentration) initially set to 1 inside a droplet of radius $R_1 = 3$ and zero elsewhere, nucleation of a droplet at the centre of the system is observed. Droplet formation occurs for any value of the activity ζ. This clustering phenomenon is due to the interplay between myosin contraction and the cross diffusion term proportional to B in Eq. (6), which recruits myosin to regions of high actin concentration. Similar results are obtained with ϕ fluctuating around a uniform value. In all cases, we observe the formation of a single droplet in steady state. Some snapshots of the evolution of the actin density field ρ are reported in Figure 1, together with the steady state contour plots of both ρ and ϕ.

In addition, for every value of the parameter G there is a critical value of activity ζ for which motion occurs. To become motile, the droplet first needs to polarise, breaking the circular symmetry in the myosin distribution. The asymmetry in ϕ can be quantified by analysing the quantity $(\phi(x) - \phi(-x))$, with x a position along a line oriented with the direction of motion, and passing through

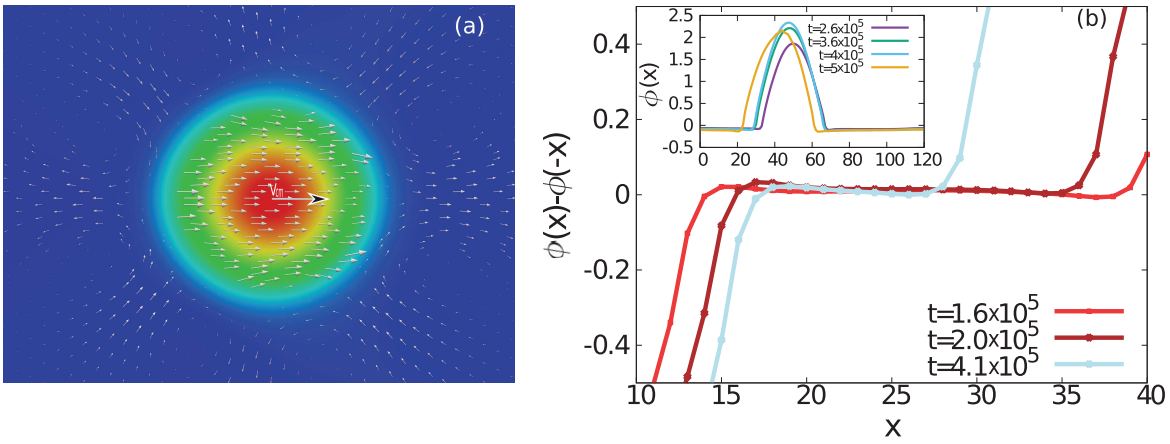

Figure 2: **(a)** Contour plot of the density ρ with superimposed velocity field, for $G = 0.88$ and $\zeta = 0.3$. The colour code here is the same of that displayed in Figure 1. **(b-main figure)** Plot of the quantity $\phi(x) - \phi(-x)$, at different times, and **(b-inset)** ϕ profiles along the x-direction at different times, for the same case of figure **(a)**. The cyan curve corresponds to the time when the droplet starts moving along the x-direction.

the centre of mass of the actin droplet. For an isotropic droplet, we expect $(\phi(x) - \phi(-x))$ to be identically zero. Figure 2(b) shows how the myosin field asymmetry develops over time for $G = 0.88$ and $\zeta = 0.3$ (a case for which we have motion). At early times ϕ is nearly symmetric (red curve in the main plot), whereas later myosin redistributes until an asymmetric steady state is reached, and the droplets starts to move (brown curve in the inset of Figure 2(b)).

Figure 2(a) also shows the velocity field of our compressible active system. Inside the droplet, the active contractily-driven flows rearrange to give a simple directed flow. There is an opposing flow outside the droplet, which is required for overall momentum conservation (as there are no boundaries or other momentum sinks). The counteracting flow involves a number of vortices which upon azymuthal averaging give a net flow in the direction opposing that of the droplet motion. Whilst vortex patterns are associated with spurious microcurrents in a passive phase-separated systems in lattice Boltzmann simulations [15], the magnitude of the flow is over an order of magnitude larger in our active case, and the pattern is different as the vortices in front and behind of the droplet are much larger (we also noted that the spurious passive and the active azymuthal flows are also fitted by different functional forms).

In experiments with cell swimming in a viscous fluid, for instance in a matrigel, the environment is fully 3-dimensional. It is therefore of interest to ask whether contraction-driven flows can rearrange to yield motility in a periodic 3D geometry. To answer this question, we performed simulations in a cubic domain of size $L = 128$. Remarkably, we find that also in 3D droplets – again assembled through myosin-mediated contraction of the compressible actin fluid – become self-motile for sufficiently strong activity. Intriguingly, the solvent flow counteracting droplet motion has now a different form (Figure 4). Two vortex−like structures originate from the poles perpendicular to the migration axis and converge toward the droplet rear, while the outer fluid is pushed away in front of the droplet. This pattern is similar both to that observed experimentally in cells "swimming" in 3D matrigel [7], and to that reported in previous numerical simulations of a self-motile active-liquid crystal droplet [16]. The emergence of this flow patterns is interesting, as our model is significantly

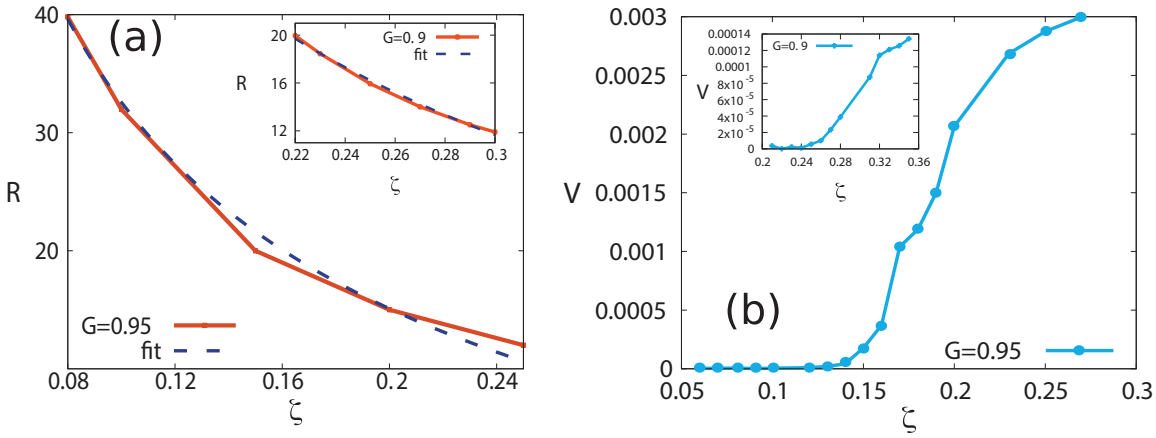

Figure 3: **(a)** Critical value of the radius of the droplet R_c as activity varies (continuous curves), for $G = 0.95$ **(main figure)**, and $G = 0.9$ **(inset)**, and the result of the fit (dashed lines) with the proportionality law reported in the text(Eq. 7). **(b)** Steady state center of mass velocity V as activity varies, for $G = 0.95$ **(main figure)**, and $G = 0.9$ **(inset)**.

simpler than the ones previously considered. We interpret the similarity in the flow patterns far from the droplet as due to the fact that the dilute actomyosin background within which the droplet moves may be viewed as an essentially passive viscous polymeric fluid (such as matrigel).

We argue that the mechanism giving rise to the symmetry-breaking instability of a non−motile configuration and ensuring directional motility of a self-propelling cell, is a positive feedback loop, closely related to the one leading to actin accumulation (Figure 1). Here, after *e.g.* a fluctuation in actin density creates an asymmetry in gradients, the flow generated by contraction is also asymmetrical, and recruits motors faster along the regions where gradients are steeper. This leads to further asymmetric contraction, and to a motile pattern due to the flow imbalance, hence creating an autocatalytic effect [17]. The coupling leads to build motor concentration, which is limited by surface tension and diffusion, resisting the runaway and providing a compensating term which is necessary to achieve a steady state. The droplet breaks symmetry and becomes motile when the activity parameter exceeds a threshold. The threshold behaviour originates from the fact that the total myosin stress needs to overcome the effects of actin viscosity and myosin diffusion. Increasing activity for a given value of G, or decreasing G for a given value of ζ, the droplet assumes an accentuated elliptical form.

To understand more quantitatively the effect of the model parameters on the droplet motion, we measured the radius of the self-assembled actin droplet and its velocity in steady state, as a function of the activity parameter ζ, and for different values of the parameter G. The droplet radius at the onset of motion is plotted in Figure 3(a) for two values of G ($G = 0.95$ in the main figure and $G = 0.9$ in the inset). It follows to a good approximation an inverse square root law:

$$R_c \sim \sqrt{\frac{1}{\zeta}} \,. \tag{7}$$

Such a dependency was suggested by linear stability analysis of a related problem [14].

Figure 3(b) shows a plot of the center of mass velocity versus ζ for two values of G ($G = 0.95$ in the main figure and $G = 0.9$ in the inset). A phase diagram in the ($G-\zeta$) plane is instead shown

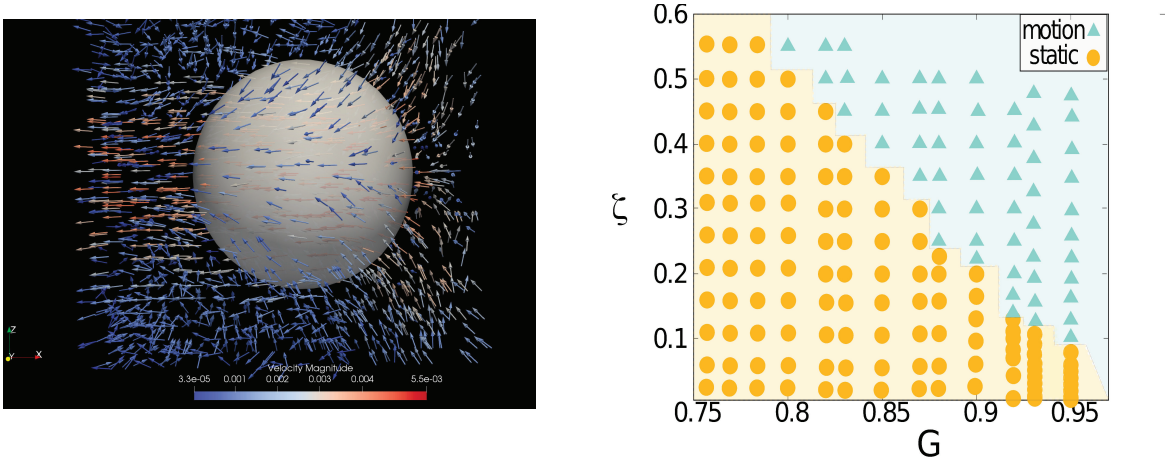

Figure 4: **(left panel)** Isosurface at $\rho = 2$, with superimposed flow field for $\zeta = 0.34$ and $G = 0.87$, in $3D$. **(right panel)** Phase diagram in the ζ (activity)-G(compressibility) plane, for the transition to motile droplet.

in Figure 4. The steady droplet velocity increases with activity and is bigger for higher values of G. At the same time, decreasing the elastic modulus of the gel – i.e., approaching the incompressible limit $G = 0$ – leads to an increase in the activity threshold above which motion is observed. This is consistent with the intuitive expectation that active isotropic contraction cannot lead to motion in this limit (as it is simply equivalent to a redefinition of the pressure). Here for the values of activity ζ we are constrained by the stability of our LB implementation, and for the values of G by the chosen values of T. We checked that fixing T to other values does not change the physical picture discussed, as it solely change the location of the transition line to a motile droplet.

3 Rotation and propulsion in 3d active chiral droplets

Understanding the outcome of the interplay between chirality and activity is an important and timely question. In stark contrast with the case of achiral active nematics, which has commanded a lot of attention in recent years, very little is known about the dynamics of chiral active systems. Previous work has mainly focused on cases where chirality only enters the system because of activity, in the form of a nonequilibrium torque dipole [18, 19]. Instead, we consider here a system which is *inherently* chiral and apolar, and so can be modelled – in the passive phase – as a cholesteric liquid crystal (CLC) [20, 21]. Specifically, here we study a $3d$ active CLC droplet with tangential orientation of the director at its surface. In this setup, an active nematic droplet can only sustain uniform rotational motion, driven by bend deformations localised around the equatorial circle of the droplet (Fig. 1). Instead, an intrinsically chiral droplet displays a much richer dynamical behaviour. First, we find that a force dipole activity enables a new motility mode, where the rotational motion of the surface defects is converted into propulsion. This mechanism requires chirality to reconfigure the pattern of surface defects. It is not possible in a nematic, where the symmetry in defect position prevents any translational motion. Second, a torque dipole activity sets up a sustained mirror rotation of two pairs of disclinations which periodically adsorb onto and depin from the droplet surface. Again, no such state can be found in an originally nematic system. We also characterise how the active flow and orientation patterns evolve as the ratio between the droplet size and pitch increases –

a procedure favouring the formation of focal conics in passive cholesterics.

3.1 Model

We considered an incompressible fluid with mass density ρ and divergence-free velocity $\mathbf{v}(\mathbf{r},t)$. To characterize the state of the system we introduced two order parameters: a scalar conserved concentration field $\phi(\mathbf{r},t)$ and the $\mathbf{Q}$-tensor that respectively account for the concentration of active material and its orientational order. The equilibrium properties of the system are described by the following Landau-De Gennes free energy functional:

$$\begin{aligned}\mathscr{F}\left[\phi,Q_{\alpha\beta}\right] = \int dV \; \Bigg[& \frac{a}{4}\phi^2(\phi-\phi_0)^2 + \frac{k_\phi}{2}(\nabla\phi)^2 \\ & + A_0\left[\frac{1}{2}\left(1-\frac{\chi(\phi)}{3}\right)\mathbf{Q}^2 - \frac{\chi(\phi)}{3}\mathbf{Q}^3 + \frac{\chi(\phi)}{4}\mathbf{Q}^4\right] \\ & + \frac{K}{2}\left[(\nabla\cdot\mathbf{Q})^2 + (\nabla\times\mathbf{Q}+2q_0\mathbf{Q})^2\right] + W(\nabla\phi)\cdot\mathbf{Q}\cdot(\nabla\phi)\Bigg] \end{aligned} \tag{8}$$

where the constants a,k_ϕ define the surface tension and the interface width among the two phases, whose minima are found in 0 and ϕ_0. The liquid crystal phase is confined in those regions where $\chi(\phi) = \chi_0 + \chi_s\phi > 2.7$, with $\chi_0 = 10\chi_s = 2.5$. The gradient terms in K_Q account for the energy cost of elastic deformations in the one-constant approximation, while $|q_0| = 2\pi/p_0$, where p_0 is the pitch of the cholesteric helix. Right-handed chirality is achieved by requiring q_0 to be positive. Tangential anchoring is obtained for $W < 0$. The dynamical equations governing the evolution of the system are: (i) a convection-diffusion equation for ϕ

$$\partial_t + \nabla\cdot(\phi\mathbf{v}) = \nabla\cdot\left(M\nabla\frac{\delta\mathscr{F}}{\delta\phi}\right), \tag{9}$$

where M is the mobility parameter; (ii) the Beris-Edwards equation for the $\mathbf{Q}$-tensor:

$$(\partial_t + \mathbf{v}\cdot\nabla)\mathbf{Q} - \mathbf{S}(\mathbf{W},\mathbf{Q}) = \Gamma\mathbf{H}, \tag{10}$$

where we introduced $\mathbf{W} = \nabla\mathbf{v}$ and the strain-rotational derivative

$$\mathbf{S}(\mathbf{W},\mathbf{Q}) = (\xi\mathbf{D}+\mathbf{\Omega})(\mathbf{Q}+\mathbf{I}/3) + (\mathbf{Q}+\mathbf{I}/3)(\xi\mathbf{D}-\mathbf{\Omega}) - 2\xi(\mathbf{Q}+\mathbf{I}/3)Tr(\mathbf{QW}), \tag{11}$$

with $\mathbf{D}$ and $\mathbf{\Omega}$ respectively denoting the symmetric and asymmetric part of $\mathbf{W}$. The parameter ξ controls the aspect-ratio of the liquid crystal molecules and aligning properties to the flow (we chose $\xi = 0.7$ to consider flow-aligning rod-like molecules). On the right-hand side of equation (10) Γ is the rotational viscosity and

$$\mathbf{H} = -\frac{\delta\mathscr{F}}{\delta\mathbf{Q}} + \frac{\mathbf{I}}{3}Tr\left(\frac{\delta\mathscr{F}}{\delta\mathbf{Q}}\right) \tag{12}$$

is the molecular field driving the system towards equilibrium. (iii) The Navier-Stokes equation rules the hydrodynamics of the system:

$$(\partial_t + \mathbf{v}\cdot\nabla)\mathbf{v} = \nabla\cdot\left[\sigma^{pass} + \sigma^{act}\right]. \tag{13}$$

We split the stress tensor contribution in a passive and an active term. The first one accounts for the dissipative/reactive contributions and can be expressed as the sum of the isotropic pressure $\sigma^{hydro}_{\alpha\beta} = -p\delta_{\alpha\beta}$, with p the hydrodynamic pressure and the viscous stress $\sigma^{visc}_{\alpha\beta} = 2\eta D_{\alpha\beta}$, with η the shear viscosity. The relxation dynamics of the two order parameters affect the hydrodynamics through the following passive terms:

$$\sigma^{bm} = \left(f - \frac{\delta \mathscr{F}}{\delta \phi}\right)\delta_{\alpha\beta} - \frac{\delta \mathscr{F}}{\delta(\partial_\beta \phi)}\partial_\alpha \phi, \tag{14}$$

where f is the free energy density,

$$\sigma^{el}_{\alpha\beta} = -\xi H_{\alpha\gamma}\left(Q_{\gamma\beta} + \frac{1}{3}\delta_{\gamma\beta}\right) - \xi\left(Q_{\alpha\gamma} + \frac{1}{3}\delta_{\alpha\gamma}\right)H_{\gamma\beta} + 2\xi\left(Q_{\alpha\beta} - \frac{1}{3}\delta_{\alpha\beta}\right)Q_{\gamma\mu}H_{\gamma\mu} + Q_{\alpha\gamma}H_{\gamma\beta} - H_{\alpha\gamma}Q_{\gamma\beta}. \tag{15}$$

The active stress tensor is given by:

$$\sigma^{act}_{\alpha\beta} = -\zeta\phi Q_{\alpha\beta} - \bar{\zeta}\varepsilon_{\alpha\mu\nu}\partial_\mu(\phi Q_{\nu\beta}). \tag{16}$$

This is explictly derived by coarse-graining the force and the torque dipoles exerted by the swimmers.

The dynamical equations have been integrated by means of a hybrid lattice Boltzmann (LB) method.

3.2 Cholesteric droplet with active force dipoles: screwlike propulsion

We now consider the case of a cholesteric droplet, still with active force dipoles only. The two key control parameters are now θ and N. For a fixed value of N, increasing ζ again leads to three possible regimes, as in the nematic limit. For sufficiently large cholesteric power (e.g., $N = 2$, Fig. 5), the first active regime encountered is, however, fundamentally different from the rotating phase of active nematics. Now the surface defect pattern is a pair of nearby $+1$ defects, reminiscent of a *Frank-Price structure* which is seen in passive cholesterics, but only with much larger N ($N \geq 5$ [21]). The configuration of director field which we observe is known as *radial spherical structure* [20, 22], with some additional distortions in the cholesteric layers due to activity (as suggested by the inset in Fig. 5g that gives an insight into the cholesteric arrangement in the interior of the droplet). There is a suggestive analogy between this structure and a magnetic monopole – representing the radial orientation of the helical structure at the droplet centre – with its attached *Dirac string* [23, 22], joining the centre of the droplet with the defect pair. In our simulations the latter represents the region of maximal layer distortion and energy injection, as suggested by the intensity of the velocity field, plotted in Fig. 5g.

The two surface defects rotate around each other: as they do so, the pair periodically separates and reconvenes. At the same time, the droplet undergoes a global rotation with oscillating angular velocity (Fig. 5h). Remarkably, this time the rotation is accompanied by a translation along the direction of the rotation axis – thereby resulting in a screwlike motion, with the axis of the rototranslation parallel to the *Dirac string*. This motility mode is compatible with the chiral symmetry of the system, which introduces a generic non-zero coupling between rotations and translations. Strong deformations induced by the two close rotating +1 defects are responsible of the intense flows that develops internally at the droplet and is maximum at the rear (see Fig. 5g) thus powering propulsion.

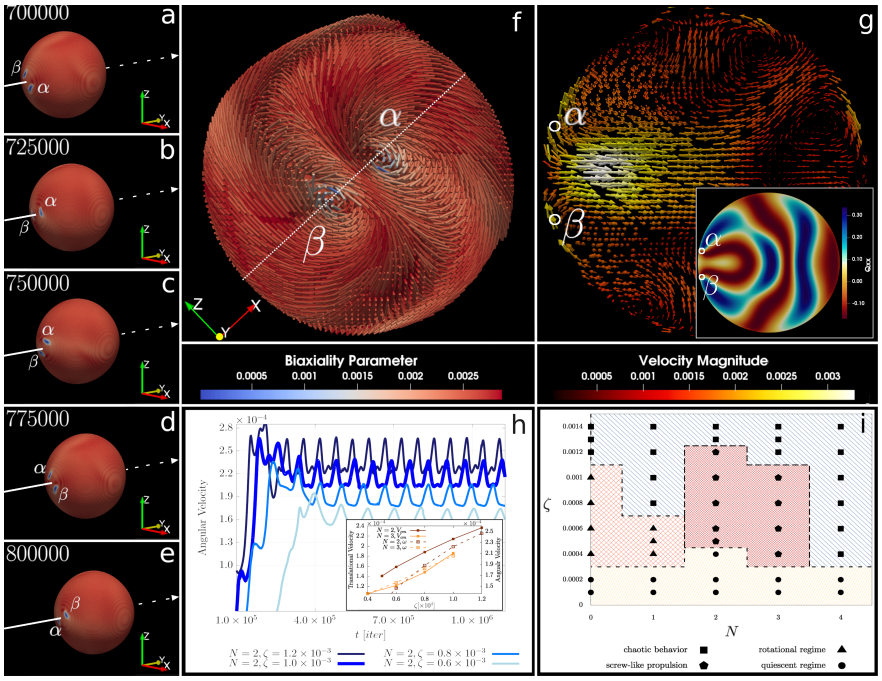

Figure 5: *Screw-like propulsion in a chiral droplet with active force dipoles.* Panels (a-e) show snapshots at different times of a chiral active droplet for the case at $N = 2$ and $\zeta = 10^{-3}$. The contour-plot of the biaxility parameter on the droplet surface serves to identify the position of the two $+1$ defects, labelled with greek characters α and β, whose configuration can be appreciated by looking at panel (f). The screw-like rotational motion generates a strong velocity field in the interior of the droplet in proximity of the two defects. The velocity field has been plotted in panel (g) on a plane transversal to the plane of rotation of the two defects (dashed line in panel (f)). The inset shows the contour plot, on the same plane, of the Q_{xx} component of the Q-tensor, exhibiting an arrangement similar to the *radial spherical structure*. Panel (h) shows the time evolution of the angular velocity of the droplet for some values of ζ. The inset shows the mean angular velocity and the translational velocity of the droplet as a function of ζ both for $N = 2$ and $N = 3$. Panel (i) summarizes the droplet behavior as a function of ζ and N.

Symmetry of the flow corresponds to that of a macroscopic pusher. Mechanistically, therefore, activity is required to power droplet rotation, and chirality is needed to couple rotation to motion. As the motion is screwlike, the linear and the angular velocity are proportional to each other – a similar argument to that used for active nematics also shows that they should both scale approximately linearly with θ, and we found this to hold for our simulations (Fig. 5h, inset).

A phase diagram in a portion of the (N, ζ) plane is shown in Fig. 5i. The results, not depending on the (random) initial conditions, show that for small activity the droplet sets into a quiescent regime indipendently of the cholesteric power: this is characterized by weak bending deformation of the LC network on the droplet surface, which are not enough to power any self-sustained motion. As activity is increased different behaviors arise: for null or weak cholesteric power ($N \leqslant 1$) stationary rotational motion sets up while screwlike propulsion needs the defects to relocate to one hemisphere creating a dipolar pattern. This is found to be only possible for a limited range of ζ and only for $N = 2, 3$. Indeed, at higher cholesteric power ($N \geqslant 4$), the droplet sets into the chaotic phase even at

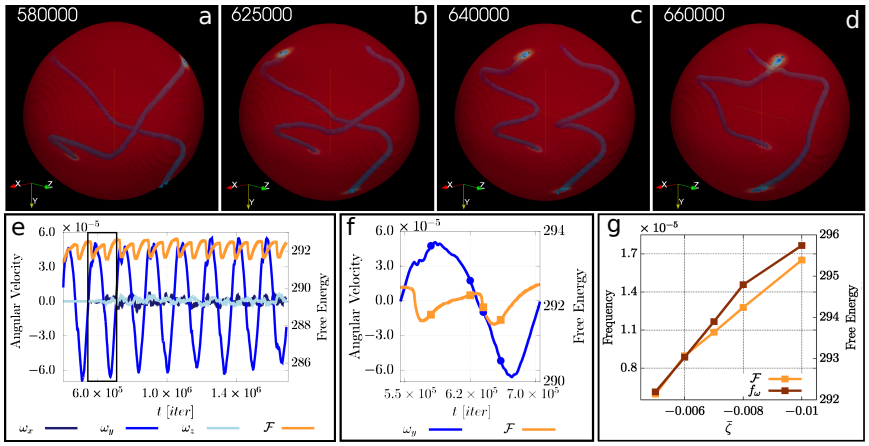

Figure 6: *Disclination dance in a chiral droplet with active torque dipoles.* Panels (a-d) show snapshots of the droplet and the disclination lines for the case at $N = 1$ and $\bar{\zeta} = -5 \times 10^{-3}$. The four $+1/2$ defects rotate in pairs in opposite directions (top defects rotate anti-clockwise, while bottom defects rotate oppositely). As the defects rotate the two disclination lines first create a link (b), then they recombine (c) and finally relax into a configuration close to the initial one (a) but rotated. The angular velocity, null on average, oscillates from positive to negative values as shown in panel (e). Here the time evolution of the free energy shows that $\mathscr{F}$ oscillates with a double frequency. Inset shows the behavior of ω_y and $\mathscr{F}$ in the region framed with the black box. Marked dots here denote the points corresponding to the snapshots.

intermediate activity, a regime characterized by defect nucleation and disordered droplet motility that can be found at any N for sufficiently large values of ζ.

3.3 Cholesteric droplets with active torque dipoles: rotation and disclination dance

We next consider the case of a cholesteric droplet with active torque dipoles. These are able to introduce a nonequilibrium twist in a nematic droplet [24], whose handedness may reinforce or oppose the handedness of the thermodynamic twist, which is determined by q_0. The strength of the nonequilibrium twist can be measured by the dimensionless number $\bar{\theta} = |\bar{\zeta}|R/K$, whilst that of the equilibrium one can be assessed by N.

We find that the most interesting dynamics, in the case of a right-handed twist ($q_0 > 0$), occurs for $\bar{\zeta} < 0$ (torque dipole corresponding to bottle cap opening, leading to a conflict between the nonequilibrium and equilibrium twist). In this situation, for $N = 1$, we find that the droplet is pierced by two disclination lines which end in $+1/2$ surface defects at $\bar{\zeta} = -5 \times 10^{-5}$. The droplet regularly alternates opposite sense rotations, along $\pm\hat{y}$, which are tightly regulated by the disclination dynamics (Fig. 6). The helical axis is here approximately parallel to $\hat{z}$, with the director almost parallel to $\hat{x}$ in the centre of the droplet.

At the beginning of the rotation cycle shown in Fig. 6, the disclinations wind once around each other in a right-handed fashion. Equivalently, if we were to orient both the disclinations along the positive $\hat{y}$ axis, we can associate the single crossing visible in the projection of Fig. 6a with a positive writhe [25] (as the top disclination can be superimposed on the bottom one via an anticlockwise rotation). As the system evolves, due to the internal torque dipoles, the pair of surface defects in the top hemisphere rotates counterclockwise, while that in the bottom hemisphere rotates clockwise

(Fig. 6b). This motion increases the winding of the disclinations, until they rewire to form two separate right-handed helices (Fig. 6c – if we were to extend the two disclinations along $\hat{z}$, they would be unlinked). The regular switches in the sense of droplet rotation beat the time of the disclination dance visualised in Fig. 6a-d. Rotation inversion occurs just at the time when the defect rewiring happens as the effect of the top/bottom asymmetry in the disclination configuration: these are regions of strong deformation leading to greater energy injection, thus strengthening the vortical flow in the corresponding emisphere and leading to the consequent oscillation of the angular velocity. We find that the evolution of the angular velocity mirrors that of the overall free energy of the system, with a small time delay: we argue that this is because the stress stored in the elastic deformations plays a large role in powering the motion. Moreover, the frequency of the free-energy oscillation is twice that of the angular velocity f_w (see panels (e-f)), a behavior in line with the fact that configurations in panel (a) and (d) are specular with respect to the rotation plane and energetically equivalent.

Unlike in the active nematic case, where rotation is powered by force dipoles, here the dynamics is driven by torque dipoles. The different physics leaves a signature in the scaling of the (maximal) angular velocity, which now can be estimated as $|\bar{\zeta}|/R$ from dimensional analysis. We confirmed this behavior simulating cholesteric droplets of different radius, ranging from $R = 18$ to 32, keeping fixed the pitch of the cholesteric helix $p_0 = 64$.

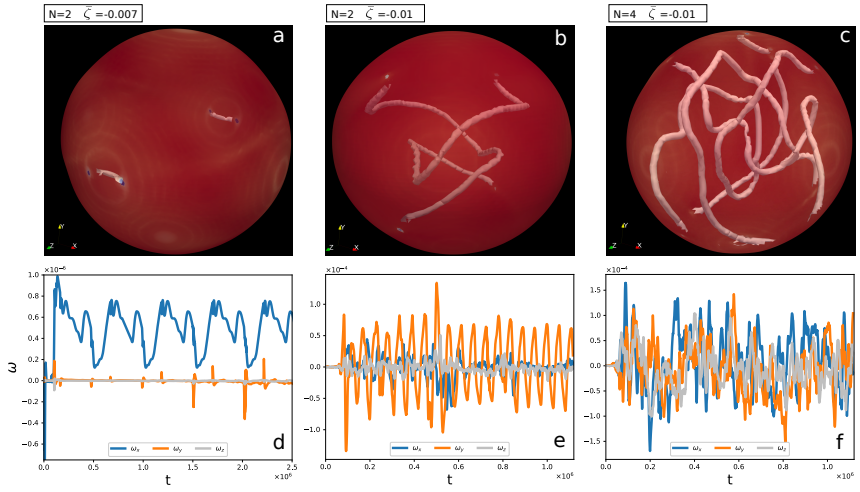

Figure 7: *Active torque dipoles.* Panel a shows a snapshot of the droplet and the disclination lines for the case at $N = 2$ and $\bar{\zeta} = -7 \times 10^{-3}$. In this case the droplet sets into rotational motion (notice the difference of the order of magnitude of the angular velocity in panel d with respect to the analogue cases presented in the main text for a droplet fueled by force dipoles only). Panel b and e show the case at $N = 2$ and $\bar{\zeta} = -10^{-2}$, characterized by the dancing of the disclination lines. Panel c shows a snapshot of the droplet and its disclination lines for the case at $N = 4$ and $\bar{\zeta} = -10^{-2}$, in the chaotic regime – see panel f – characterized by nucleation of surface defects (panel c).

The scenario concerning the properties of a cholesteric droplet fueled by torque dipoles, is highly sensitive to both the active doping and the twisting number N. Indeed, the dynamics described so far at $N = 1$ is stable only for a limited range of activity ($5 \times 10^{-3} \leqslant |\bar{\zeta}| \leqslant 12 \times 10^{-3}$). Small values of $|\bar{\zeta}|$ ($< 5 \times 10^{-3}$), are not enough to excite the splitting of the two boojums and generate instead bending deformations of the LC pattern at $N = 1$, similar to those shown in Fig. **??**a. In this case the droplet sets into a stationary rotational motion characterized by small angular velocity

($|\boldsymbol{\omega}| \sim \mathcal{O}(10^{-6})$) (7). If activity exceeds a critical threshold, $|\bar{\zeta}| > 12 \times 10^{-3}$, nucleation of further defects on the droplet surface leads to droplet deformation with consequent chaotic dynamics (Supp. Fig. 1). The competition between active and equilibrium chirality has important effects when N is changed. Indeed, a further key dimensionless number to determine the behaviour of a cholesteric droplet with active torque dipoles is $\bar{\zeta}/(q_0 K)$, or equivalently, the ratio between the pitch and the "active torque length" $K/\bar{\zeta}$. The latter can be thought of as the nonequilibrium pitch, or the modulation in twist due to the action of the active flow. We would then expect that for larger q_0 (i.e., larger N at fixed R), a rotating regime as in Fig. 6 can be obtained by increasing $\bar{\zeta}$ (Supp. Fig. 1). Our simulations confirm, indeed, that the range of stability of stationary rotation widens as N is increased, while the set up of the mirror rotation regime moves towards more intense $|\bar{\zeta}|$. Nevertheless, if $N \geqslant 4$, the droplet directly moves from the rotational to the chaotic regime, analogously to what happens in a cholesteric droplet fueled by force dipoles only.

It is notable that the disclination dance which we observe at intermediate $|\bar{\zeta}|$ is also reminiscent of that seen experimentally in active nematic shells [26, 27, 28] made up of microtubule-molecular motor mixtures. Despite the confined geometry is different, our results suggest that the underlying mechanism powering rotation observed in the aforementioned studies, may be related to torque rather than force dipoles.

Published Papers

1. **G. Negro**, L.N. Carenza, G. Gonnella, A. Lamura, G. Negro, A. Tiribocchi, Rheology of active polar emulsions: from linear to unidirectional and inviscid flow, and intermittent viscosity, **Soft Matter**, (2019).
2. **G. Negro**, L.N. Carenza, P. Digregorio, G. Gonnella, A. Lamura, **Physica A** 503, 464 (2018)
3. **G. Negro**, A. Lamura, G. Gonnella and D. Marenduzzo, Hydrodynamics of contraction-based motility in a compressible active fluid, **EPL**, 127 (2019) 58001.
4. **G. Negro**, S. Busuioc, V. E. Ambruş, G. Gonnella, A. Lamura and V. Sofonea, Comparison between isothermal collision-streaming and finite-difference lattice Boltzmann models, **International Journal of Modern Physics C**, 127 (2019).
5. L.N. Carenza, G. Gonnella, A. Lamura, **G. Negro**, A. Tiribocchi, **Eur. Phys. J. E** 42: 81 (2019).
6. L.N. Carenza, G. Gonnella, D. Marenduzzo, **G. Negro**, Rotation and propulsion in 3d active chiral droplets, On press **PNAS** (2019).
7. L.N. Carenza, A. Lamura, G. Gonnella, **G. Negro**, Dynamically asymmetric and bicontinuous morphologies in active emulsions, **International Journal of Modern Physics C**, (2019).

Proceedings

1. G Negro, LN Carenza, P Digregorio, G Gonnella, A Lamura, In silico characterization of asymmetric active polar emulsions, AIP Conference Proceedings 2071 (1), 020012

Experiences abroad

1. October-December 2017 HPC Europa3 grant, Edinburgh, under the supervision of Prof. D. Marenduzzo.
2. March-June 2019 HPC Europa3 grant, Edinburgh, under the supervision of Prof. D. Marenduzzo.

Conferences and Schools

1. INTERNATIONAL SUMMER SCHOOL FPSP XIV, 16-29 JULY, 2017
2. Flowing Matter 2016, $11/01/17 - 15/01/17$ Porto, Portugal.
3. TIM18, $26/05/18 - 28/05/18$ Timisoara, Romania.
4. DSFD, $25/06/18 - 30/06/18$ Worchester, USA.

5. Soft matter days, 14/09/18 – 15/09/18 Padova, Italy.
6. APS/DFD, 04/11/18 – 06/11/18 Atlanta, USA.
7. Fismat19, 30/09/2019 – 04/10/2019 Catania, Italy.

References

[1] D. Wedlich. *Cell Migration in Development and Disease*. Wiley, 2006.

[2] J. Prost J.F. Joanny H. Turlier, B. Audoly. Furrow constriction in animal cell cytokinesis. *Biophysical Journal*, 106:114, 2014.

[3] E. Barnhart, C. Lee, K. Keren, A. Mogilner, and J.A. Theriot. An adhesion-dependent switch between mechanisms that determine motile cell shape. *PLOS Biology*, 9(5):1–19, 05 2011.

[4] G.M. Allen J.A. Theriot E. Barnhart, K.C. Lee and A. Mogilner. Balance between cell-substrate adhesion and myosin contraction determines the frequency of motility initiation in fish keratocytes. *Proceedings of the National Academy of Sciences*, 112(16):5045–5050, 2015.

[5] E. Tjhung, A. Tiribocchi, D. Marenduzzo, and M.E. Cates. A minimal physical model captures the shapes of crawling cells. *Nat. Commun.*, 6:5420, 2015.

[6] D. Bray. *Cell Movements: From Molecules to Motility*. Garland Pub., 2001.

[7] R. Poincloux, O. Collin, F. Lizarraga, M. Romao, M. Debray, M. Piel, and P. Chavrier. Contractility of the cell rear drives invasion of breast tumor cells in 3d matrigel. 108:1943–8, 02 2011.

[8] H. Keller, A.D. Zadeh, and P. Eggli. Localised depletion of polymerised actin at the front of walker carcinosarcoma cells increases the speed of locomotion. *Cell Motility and the Cytoskeleton*, 53(3):189–202, 2002.

[9] M.C. Marchetti, J.-F. Joanny, S. Ramaswamy, T.B. Liverpool, J. Prost, M. Rao, and R.A. Simha. Hydrodynamics of soft active matter. *Rev. Mod. Phys.*, 85:1143, 2013.

[10] S. Fürthauer, M. Strempel, S. W. Grill, and F. Jülicher. Active chiral fluids. *The European Physical Journal E*, 35(9):89, Sep 2012.

[11] E. Tjhung, D. Marenduzzo, and M. E. Cates. Spontaneous symmetry breaking in active droplets provides a generic route to motility. *Proc. Natl. Acad. Sci. U.S.A.*, 109(31):12381–12386, 2012.

[12] G. De Magistris, A. Tiribocchi, C.A. Whitfield, R.J. Hawkins, M.E. Cates, and D. Marenduzzo. Spontaneous motility of passive emulsion droplets in polar active gels. *Soft Matter*, 10:7826–7837, 2014.

[13] P. Recho, T. Putelat, and L. Truskinovsky. Contraction-driven cell motility. *Phys. Rev. Lett.*, 111:108102, Sep 2013.

[14] T. Le Goff, B. Liebchen, and D. Marenduzzo. Actomyosin contraction induces droplet motility. *arXiv:1712.03138*, 2003.

[15] A. J. Wagner. The origin of spurious velocities in lattice boltzmann. *International Journal of Modern Physics B*, 17(01n02):193–196, 2003.

[16] E. Tjhung, A. Tiribocchi, D. Marenduzzo, and M.E. Cates. A minimal physical model captures the shapes of crawling cells. *Nature Communications*, 6:5420, 2015.

[17] M. Mayer, M. Depken, J.S. Bois, F. Jülicher, and S. Grill. Anisotropies in cortical tension reveal the physical basis of polarizing cortical flows. *Nature*, 467:617, November 2010.

[18] E. Tjhung, M.E. Cates, and D. Marenduzzo. Contractile and chiral activities codetermine the helicity of swimming droplet trajectories. *Proc. Natl. Acad. Sci.*, 114(18):4631–4636, 2017.

[19] A. Maitra and M. Lenz. Spontaneous rotation can stabilise ordered chiral active fluids. *Nat. Commun.*, 10, 2019.

[20] David Seč, Tine Porenta, Miha Ravnik, and Slobodan Žumer. Geometrical frustration of chiral ordering in cholesteric droplets. *Soft Matter*, 8:11982–11988, 2012.

[21] T. Leon and F. Nieves. Drops and shells of liquid crystal. *A. Colloid Polym Sci*, 289(4):345–359, 2011.

[22] Ye Zhou, Emre Bukusoglu, José A. Martínez-González, Mohammad Rahimi, Tyler F. Roberts, Rui Zhang, Xiaoguang Wang, Nicholas L. Abbott, and Juan J. de Pablo. Structural transitions in cholesteric liquid crystal droplets. *ACS Nano*, 10(7):6484–6490, 2016. PMID: 27249186.

[23] M. V. Kurik and O. D. Lavrentovich. Negative-positive monopole transitions in cholesteric liquid crystals. *Soviet Journal of Experimental and Theoretical Physics Letters*, 35:444, May 1982.

[24] E. Tjhung, M.E. Cates, and D. Marenduzzo. Nonequilibrium steady states in polar active fluids. *Soft Matter*, 7:7453–7464, 2011.

[25] A.D. Bates, S.B.S.A.D. Bates, A. Maxwell, and H.D.B.C.A. Maxwell. *DNA Topology*. Oxford bioscience. Oxford University Press, 2005.

[26] Felix C. Keber, Etienne Loiseau, Tim Sanchez, Stephen J. DeCamp, Luca Giomi, Mark J. Bowick, M. Cristina Marchetti, Zvonimir Dogic, and Andreas R. Bausch. Topology and dynamics of active nematic vesicles. *Science*, 345(6201):1135–1139, 2014.

[27] R.Z. Zhang, M. Ye Rahimi, and J.J. de Pablo. Dynamic structure of active nematic shells. *Nature Communications*, 7:13483, 2016.

[28] Pau Guillamat, Žiga Kos, Jérôme Hardoüin, Jordi Ignés-Mullol, Miha Ravnik, and Francesc Sagués. Active nematic emulsions. *Science Advances*, 4(4), 2018.